## CFD modeling of condensing steam ejectors: Comparison with an experimental test-case

(Article begins on next page)

16 August 2024

# CFD modeling of condensing steam ejectors: comparison with an experimental test-case

**Federico Mazzelli[*], Francesco Giacomelli, Adriano Milazzo**

Department of Industrial Engineering, University of Florence,

via di Santa Marta, 3 – 50139 FIRENZE (ITALY)

## Abstract

In the present paper, a numerical model for the simulation of wet-steam flows has been developed and implemented within a commercial CFD code (ANSYS Fluent) via user defined functions. The scheme is based on a single-fluid approach and solves the transport equations for a homogeneous mixture coupled with conservation equations for the droplets number and liquid volume fraction. The model is validated against a steam nozzle test-case and then compared with experimental data from a steam ejector with a significant amount of generated liquid phase. The simulations show a good agreement both in terms of mass flow rates and pressure profile data. Some of the modeling assumptions are also reviewed and discussed.

**Keywords**: Wet-Steam; CFD; Experimental Test-Case; Steam Ejector; Non-Equilibrium Condensation

## Nomenclature

| Latin letters | | Greek letters | |
|---|---|---|---|
| $a$ | Speed of sound [m s$^{-1}$] | $\alpha$ | Volume fraction [-] |
| $B$ | Second virial coefficient [m$^3$ kg$^{-1}$] | $\beta$ | Mass fraction [-] |
| $C$ | Third virial coefficient [m$^6$ kg$^{-2}$] | $\Gamma$ | Liquid mass generation rate [kg m$^{-3}$ s$^{-1}$] |
| $c$ | Specific heat capacity [J kg$^{-1}$ K$^{-1}$] | $\gamma$ | Specific heat ratio [-] |
| $G$ | Gibbs Free-Energy [J] | $\eta$ | Droplets per unit volume mixture [m$^{-3}$] |
| $h_{lv}$ | Latent heat [J kg$^{-1}$] | $\lambda$ | Thermal conductivity [W m$^{-1}$ K$^{-1}$] |
| $J$ | Nucleation rate [s$^{-1}$ m$^{-3}$] | $\xi$ | Kantrowitz non isothermal correction |
| $k_b$ | Boltzmann constant [J K$^{-1}$] | $\rho$ | Density [kg m$^{-3}$] |
| $k$ | Turbulent kinetic energy [m$^2$ s$^{-2}$] | $\sigma$ | Surface tension [J m$^{-2}$] |
| $l$ | Molecular mean free path [m] | $\tau$ | Shear stress [Pa] |
| $m$ | Mass [kg] | $\varphi_{ss}$ | Supersaturation ratio [-] |
| $n$ | Droplets per unit mass of mixture [kg$^{-1}$] | $\omega$ | Specific dissipation rate [s$^{-1}$] |

---

[*] Corresponding author: federico.mazzelli@unifi.it – 0039 055 2758740

| $p$ | Pressure [Pa] | *Subscripts* | |
|-----|---------------|--------------|---|
| $q_c$ | Accommodation factor | $d$ | Droplet |
| $R$ | Specific gas constant [J kg$^{-1}$ K$^{-1}$] | $m$ | Mixture, molecule |
| $r$ | Radius [m] | $v$ | Vapor |
| $t$ | Time [s] | | |
| $T$ | Temperature [K] | | |
| $u$ | Velocity [m s$^{-1}$] | | |

# 1. Introduction

Non-equilibrium condensation of steam occurs in many jet and turbomachinery devices, such as supersonic nozzles, ejectors and low pressure stages of steam turbines. Normal operation of these devices involves flow expansions that leads to thermodynamic states that are well within the saturation dome. Due to the very limited residence time, however, thermodynamic equilibrium is not maintained and the water vapor reaches high levels of supercooling. At a certain degree of steam expansion, the vapor state abruptly collapses and condensation takes place as a shock-like disturbance, called the "condensation shock" [1]. This sudden change in the state of aggregation leads to an instantaneous and localized heat release that increases the pressure and temperature and reduces the Mach number. Moreover, the condensation shock implies large temperature differences between the phases that cause irreversibilities. Downstream of the condensation shock, the flow contains a considerable number of small liquid droplets (of the order of $10^{19}$/dm$^3$, [2]) that can interact in non-trivial ways with the carrier phase.

To date, CFD simulations of wet-steam flows have proved to achieve a quite good agreement for the steam condensation within transonic nozzles [3], both in terms of pressure and droplet size trends. However, the same may not hold true in ejector applications where the interaction between droplets, shocks and shear layers may introduce many unpredictable effects. In this respect, most of the numerical studies on condensing steam ejectors have been accomplished through single-phase, ideal-gas simulations (e.g., [4]) and very few examples of CFD using wet steam models exist (see for instance, [5], [6]). This lack of detailed simulations of condensing steam ejectors provides motivations for this study.

In order to accurately validate numerical simulation on ejector applications, the comparison with experimental data should be made by considering both global and local parameters. Unfortunately, articles reporting these type of data appears to be very few. In particular, the study of Chunnanond and Aphornratana [7], and the subsequent work of Sriveerakul *et al.* [4], provide results for the entrainment ratios and pressure profiles along the ejector walls. However, no information on the separate primary and secondary mass flow rates is given, which makes difficult the assessment of numerical results. In this work, the validation of the developed model is made by comparing the simulation results against two different experimental test-cases, the converging-diverging nozzle from Moses and Stein [8] and the supersonic steam ejector studied by Al-Doori [9] and Ariafar *et al* [5], who provide data for both mass flow rates and wall pressure profiles.

## 2. Numerical Model

In the past decades, several methods have been devised to simulate wet steam flows, with different levels of complexities and accuracy. The simplest and perhaps most used is the so-called "single-fluid" approach. This is basically a fully Eulerian scheme that assumes the liquid phase to be uniformly dispersed within the vapor volume. The mass, momentum and energy conservation equations are written for the homogeneous two-phase mixture and two further equations describes the conservation of the droplets number and liquid mass within the computational domain. This method is commonly employed by commercial codes (e.g. ANSYS Fluent or CFX) and has been used by several research teams [5] [6] [10].

A second method, called the "two-fluid" approach, is very similar to the previous one, with the exception that the conservation equations are solved for the two phases separately. This can result in greater accuracy thanks to the possibility of describing the energy and force exchange between the phases. On the other hand, modeling the interphase interaction is a complex task that can potentially lead to larger uncertainties than with the use of simpler models (especially in ejectors, where the wet-steam flows across shear layers and shocks). The two-fluid method has been investigated by many authors, who have either adapted commercial codes [11] or developed in-house solvers [12] [13].

To date, wet steam models are available in many commercial CFD codes that generally feature models based on the single-fluid approach. Although these codes dispense from developing complex in-house solvers, the use of built-in models does not allow freedom in the change of model parameters and settings. This work represents an attempt to overcome this limitation through the development of a customized model within a widely used CFD commercial code. This approach has the double benefit of allowing great flexibility in the choice of the physical model and, at the same time, exploiting the capability of commercial software in terms of solver settings.

The scheme developed in this work is based on the single-fluid approach. The conservation equations for mass, momentum and energy are written for the average mixture fluid and assume the form of the conventional Navier-Stokes equations for compressible flows:

$$\frac{\partial \rho_m}{\partial t} + \frac{\partial \rho_m u_{mj}}{\partial x_j} = 0$$

$$\frac{\partial \rho_m u_{mi}}{\partial t} + \frac{\partial \rho_m u_{mi} u_{mj}}{\partial x_j} = -\frac{\partial p}{\partial x_j} + \frac{\partial \tau_{ij\_eff}}{\partial x_j}$$

$$\frac{\partial \rho_m E_m}{\partial t} + \frac{\partial \rho_m u_{mj} H_m}{\partial x_j} = \frac{\partial q_{j\_eff}}{\partial x_j} + \frac{\partial u_{mi} \tau_{ij\_eff}}{\partial x_j}$$

(1)

In eq. (1), the properties of the mixture are described by means of mass or volume weighted averages:

$$\varsigma_m = \beta \varsigma_l + (1 - \beta)\varsigma_v$$

$$\chi_m = \alpha_l \chi_l + (1 - \alpha_l)\chi_v$$

(2)

3

128

where $\varsigma_m$ represents mixture thermodynamic properties like enthalpy, entropy, total energy, etc…, $\chi_m$ is the mixture density, molecular viscosity or thermal conductivity, $\beta$ is the liquid mass fraction and $\alpha_l$ is the liquid volume fraction. The connection between these last two quantities is straightforward:

$$\beta = \frac{m_l}{m_l + m_v} = \frac{\alpha_l \rho_l}{\alpha_l \rho_l + (1 - \alpha_l)\rho_v} \tag{3}$$

The evaluation of the mixture speed of sound requires special considerations [14], and is calculated here by means of an harmonic average:

$$a = \sqrt{\frac{1}{(\alpha_l \rho_l + \alpha_v \rho_v)\left(\frac{\alpha_l}{\rho_l a_l^2} + \frac{\alpha_v}{\rho_v a_v^2}\right)}} \tag{4}$$

Coupled with the transport equation for the mixture are the two equations for the conservation of the liquid mass and the droplets number:

$$\frac{\partial \rho_m n}{\partial t} + \frac{\partial \rho_m u_{mj} n}{\partial x_j} = \alpha_v J \tag{5}$$

$$\frac{\partial \rho_l \alpha_L}{\partial t} + \frac{\partial \rho_l u_{mj} \alpha_L}{\partial x_j} = \Gamma \tag{6}$$

where "$n$" is the number of droplets per unit mass of the mixture and it is assumed that the two phases move at the same speed (no-slip condition).

The term "$J$" in eq. ( 5 ) represents the nucleation rate, i.e., the rate of formation of new droplets per unit volume of vapor and is expressed here through the classical nucleation theory (more details can be found in [15]) modified with the Kantrowitz non-isothermal correction [16]:

$$J = \frac{q_c}{(1 + \xi)} \frac{\rho_v^2}{\rho_l} \left(\frac{2\sigma}{\pi m^3}\right)^{1/2} exp\left(-\frac{\Delta G^*}{k_b T_v}\right)$$

$$\xi = q_c \frac{2(\gamma - 1)}{(\gamma + 1)} \frac{h_{lv}}{RT_v}\left(\frac{h_{lv}}{RT_v} - \frac{1}{2}\right) \tag{7}$$

Where $q_c$ is the accommodation factor, $h_{lv}$ is the liquid-vapor latent heat, $\sigma$ is the liquid water surface tension and $\xi$ is the Kantrowitz non-isothermal correction.

This correction is needed when the rapidity of the nucleation process prevents the two phase from reaching the thermal equilibrium (i.e., $T_L = T_v$). In the case of fast transformations (or low heat transfer rate between the

4

181 phases) the temperature in the cluster becomes greater than $T_v$ due to the latent heat release. This localized heat
182 release enhances the rate at which the molecules evaporate from the cluster surface and leads to a partial
183 suppression of the critical nucleation rate $J$. The Kantrowitz' correction reproduces this phenomenon and
184 typically reduces $J$ by a factor of 50–100 [15].

185 The term $\Delta G^*$ in eq. ( 7 ) is Gibbs Free energy needed to form a stable liquid cluster (other thermodynamic
186 constants are defined in the nomenclature). Thermodynamic stability considerations lead to a simple
187 expression for $\Delta G^*$ [17]:

188

$$\Delta G^* = \frac{4}{3}\pi r^{*2}\sigma \qquad (8)$$

189

190 Where $r^*$ is the critical radius of a stable liquid cluster:

191

$$r^* = \frac{2\sigma}{\rho_l RT_v \cdot ln\varphi_{ss}}$$
$$\varphi_{ss} = \frac{P_v}{P_{sat}(T_v)} \qquad (9)$$

192

193 where $\varphi_{ss}$ is the supersaturation ratio.

194 Equations ( 7 ) - ( 9 ) give the rate at which liquid nuclei spontaneously form within the vapor stream. The
195 presence of the exponential term in eq. ( 7 ) is indicative of the shock-like nature of the condensation
196 phenomenon. Moreover, it is important to note that all the variables of equations ( 7 ) - ( 9 ) depend solely on
197 the vapor thermodynamic state.

198 In order to close the set of governing equations, it is necessary to provide a law for the liquid mass generation
199 rate per unit volume of mixture, $\Gamma$, in eq. ( 6 ). This quantity stems from two different sources:

200

$$\Gamma = \Gamma_{nuc} + \Gamma_{grow} = \alpha_v m_d^* J + \rho_m n \frac{dm_d}{dt} \qquad (10)$$

201

202 where $m_d$ is the mass of a generic liquid droplet and $m_d^*$ is its value when the liquid nucleus first forms. By
203 assuming a spherical shape for all liquid droplets, these are given by:

204

$$m_d^* = \frac{4}{3}\pi\rho_l r^{*3}$$
$$m_d = \frac{4}{3}\pi\rho_l r_d^3 = \frac{\rho_l \alpha_l}{\rho_m n} \qquad (11)$$

205

206 The first of the two terms in the RHS of eq. ( 10 ) describes the mass generated from freshly nucleated droplets.
207 This term is significant only in the first stages of the condensation process and is rapidly overtaken by the

Elimin
Elimi
Elimi
Elimi
Elimi
Elimi
Elimi

249     second addendum, $\Gamma_{grow}$, which represents the growth or shrinkage of existing droplets. Its expression requires

250     the definition of a droplet growth law. In this work we use the formulation derived by Hill following a statistical

251     mechanics approach [2] and later rearranged by Young [18]:

252

$$\frac{dr_d}{dt} = \frac{p_v}{\rho_l h_{lv}\sqrt{2\pi R T_v}} \frac{c_p + c_v}{2} \cdot (T_s(p_v) - T_v) \tag{12}$$

253

254     Equations from ( 1 ) to ( 12 ) form a closed system of equations that can be solved as long as the vapor and

255     liquid equations of state and thermodynamic properties are provided. In this respect, calculations of the non-

256     equilibrium phase-change of steam necessarily requires the description of the fluid properties in metastable

257     conditions, meaning that common tabulated properties cannot be used to this purpose. Unfortunately, there is

258     a serious lack of experimental data for the properties of steam in supercooled conditions, which is regularly

259     testified by reports of the International Association for the Properties of Water and Steam (IAPWS) [19].

260     Consequently, it is necessary to extrapolate a generic equation of state outside its normal range of validity in

261     order to describe metastable states within the saturation curve.

262     In the present work, the steam properties are calculated following the work of Young [20] who derived a Virial

263     equation of state truncated at the third term of the expansion:

264

$$p = \rho_v R T_v \cdot (1 + B\rho_v + C\rho_v^2) \tag{13}$$

265

266     where *B* and *C* are the second and third Virial coefficients. These are function of the sole temperature and their

267     expressions were calibrated to match steam data in the range between 273.16 and 1073 K. Moreover,

268     formulations for the enthalpy, entropy and specific heats are derived from the Virial equations based on a

269     procedure described by Young [20]. The steam thermal conductivity and dynamic viscosity are given by low

270     order polynomial functions of the vapor temperature obtained from interpolation of NIST dataset [21]. The

271     liquid phase properties (viz., liquid density, specific heat capacity, thermal conductivity and viscosity) are

272     calculated assuming saturation conditions and are again expressed through empirical correlations obtained

273     from NIST [21]. Finally, the water surface tension is a function of the sole temperature and is expressed

274     following Young [18].

275     The described model has been implemented within the commercial CFD package ANSYS Fluent v18.0 [22].

276     In this regard, ANSYS Fluent features a built-in Wet Steam model that exploits a specifically developed

277     density based solver. Unfortunately, it is not possible to directly modify the nucleation rate and droplet growth

278     laws of this model according to user defined schemes. Nevertheless, the set-up of a customized scheme is still

279     possible within the framework of Fluent pressure-based multiphase solver by adding a number of User Defined

280     Functions (UDF). Of these, three are needed to input the source terms for the liquid mass fraction and droplet

281     number transport equation and to enforce the expression for the diameter of the droplets. Moreover, a User

282     Defined Real Gas Model is required to implement the virial equation of state and transport properties of the

313 vapor phase. Ultimately, it may be worth to note that, although density-based solvers generally perform better,
314 pressure-based schemes have also been successfully applied for the simulations of multiphase compressible
315 flows with discontinuities (e.g. [23]). In the next section, the accuracy of the developed pressure-based scheme
316 will be assessed by comparison with results from the Fluent density based model.
317

## 3. Steam Nozzle

319 In what follows, the presented numerical model is compared against data from the well-known nozzle test case
320 of Moses and Stein [8]. The results are firstly also confronted with those obtained with the ANSYS Fluent
321 built-in wet steam model in order to benchmark the present scheme with a previously validated code (e.g., [24]
322 [25]). In this comparison, the droplet generation and growth rates equations implemented in the customized
323 model are the same as those featured by the Fluent built-in scheme. Subsequently, we address the analysis of
324 changes in some of the model's settings (e.g., the droplet growth law).
325 The computational domain for these simulations has approximately 30'000 quadrilateral cells with y+<1 along
326 the nozzle surfaces and is presented in Fig. 1. Due to the relative simplicity of the flow field (e.g., absence of
327 pressure shocks), it was possible to set-up a third order accurate QUICK scheme [26] for the spatial
328 discretization of all transport equations. A k-ω SST turbulence model is selected for all simulations.
329
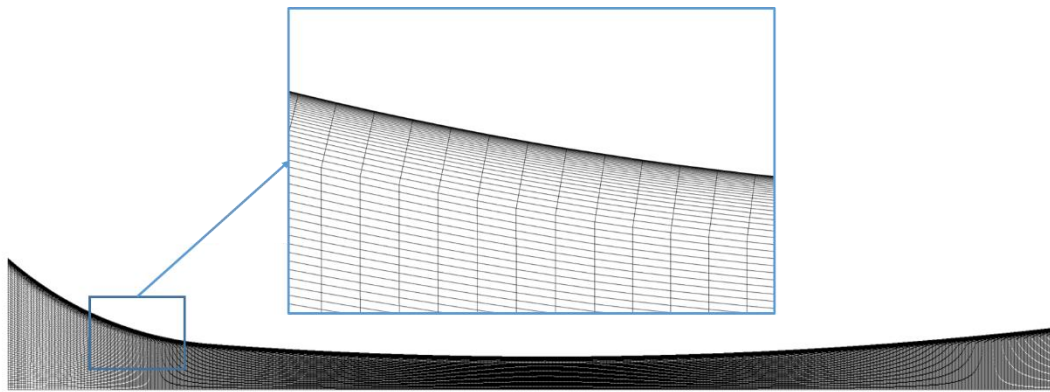


331 *Fig. 1 – Computational domain for the nozzle test-case*

333 Simulations are performed for the experiment n. 252, which has inlet total pressure of 40 kPa and inlet total
334 temperature of 101.2 K [8]. For this test, data on pressure profiles and liquid mass fraction along the axis are
335 available. Results on droplet average radius were not presented in the original paper; however, these were
336 processed by Young [18] starting from light scattering data.
337 Fig. 2 shows the normalized pressure trend along the ejector axis. The figure focuses on the region downstream
338 of the nozzle throat (located at x=8,22 cm from the nozzle inlet) where the condensation shock takes place and
339 experimental measurements are available. Clearly, the presented model overlaps with results from the Fluent
340 built-in model and both seem to capture the pressure trend with reasonable accuracy. When compared to

369 experimental values, numerical results underestimate the general pressure level and the steepness of the

370 pressure rise.

371 Fig. 2 presents also the comparison on the average droplet radii along the nozzle axis. The results show that

372 CFD predicts values that are approximately a half of the experimental. Nevertheless, it is known that for this

373 particular test-case there is a general tendency to under-predict droplet sizes by CFD models [3].

374 It is interesting to note that the numerical trends for the average radius tend to predict different slope of the

375 curve in the region where the nucleation has terminated. This difference is even more pronounced when

376 comparing the trends for the number of droplets per unit volume of mixture, as shown in Fig. 3. The figure

377 clearly shows two different trends of the numerical codes. In particular, the Fluent built-in model predicts the

378 presence of a plateau immediately downstream of the nucleation zone, whereas the developed model shows a

379 decreasing trend in this region.

380 The reason for this difference is to be found in the formulation for the droplet number conservation, eq. ( 5 ).

381 In the present study, the equation is written in term of the conservation of the droplets per unit mass of mixture,

382 which, once multiplied by the mixture density, returns the number of droplets per unit volume:

383

$$\eta = \rho_m n \tag{14}$$

384

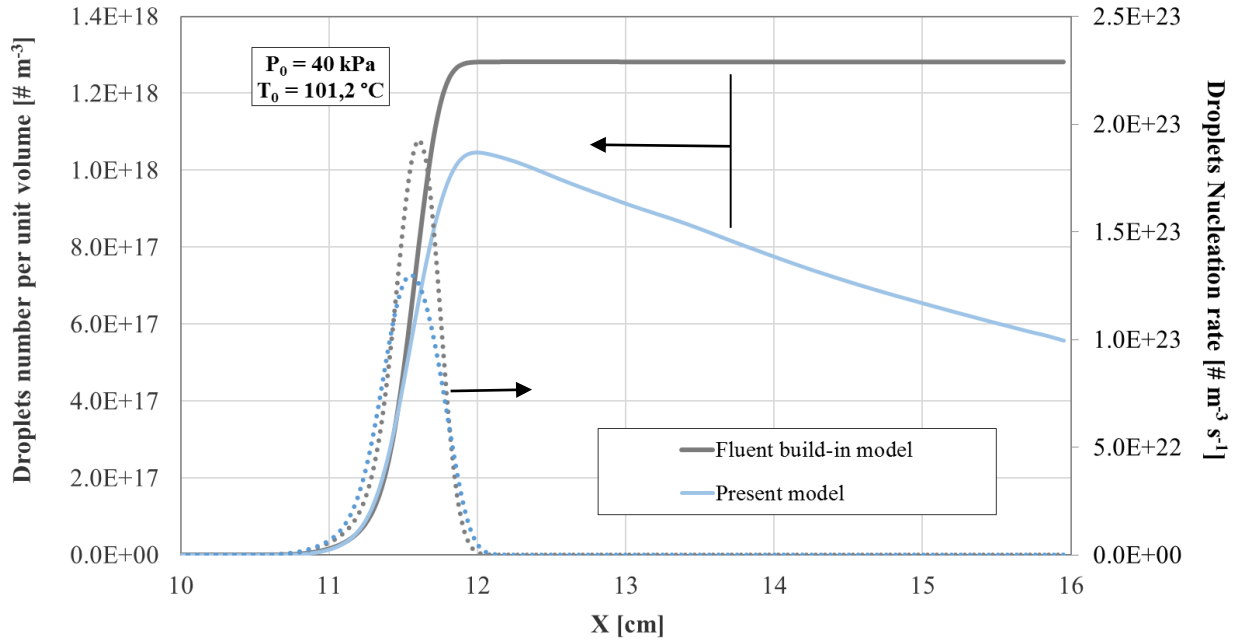385 where $\eta$ is the number of droplets per unit volume of mixture (or number density).

386 Writing eq. ( 5 ) in these terms allows the total number of droplets to be conserved in the computational domain,

387 which is simply shown by performing a volume integration of the LHS of eq. ( 5 ) (the conservation of the

388 droplet number can equally be obtained by using $\eta$ as a variable, as long as the proper corrections to the droplet

389 nucleation term, $J$, are made). Consequently, the present model improves on the Fluent built-in scheme by

390 correctly reproducing a decreasing trend for $\eta$. This is caused by the fact that the total number of nuclei $n$ is

391 constant in this region (the nucleation rate is zero) and the flow is expanding in a duct with increasingly larger

392 sections.

393



394

8
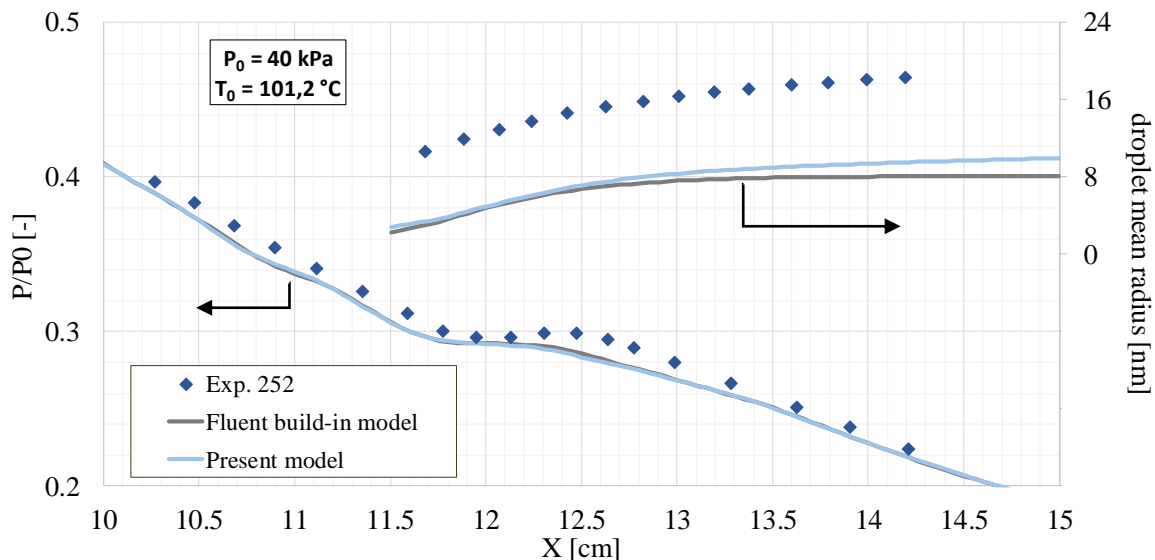
*Fig. 2 – Normalized pressure trend along the nozzle axis (bottom curves) and corresponding droplet average*

*radius (top right curves)*



*Fig. 3 – Number of droplets per unit volume of mixture along the nozzle axis (solid lines) and the*

*corresponding droplets nucleation rates (dotted lines)*

## Sensitivity to different model settings

In this section, we present an analysis of the sensitivity to some of the most influential parameters of the phase change model, i.e., the surface tension, the nucleation equation and the droplet growth law. Specifically, we first evaluate the impact of suppressing the Kantrowitz non-isothermal correction from the nucleation equation. Secondly, we describe the surface tension by using an empirical correlation from IAPWS [19]. Lastly, we analyze the use of a widely used droplet growth law that was derived by Young [18] starting from an equation obtained by Gyarmathy [27]. Its final expression is as follows [3]:

$$\frac{dr_d}{dt} = \frac{\lambda_v}{\rho_l h_{lv} r_d} \frac{\left(1 - \frac{r^*}{r_d}\right)}{\left(\frac{1}{1 + 2C_1 Kn} + 3.78(1-v)\frac{Kn}{Pr}\right)} \cdot (T_s(p_v) - T_v) \tag{15}$$

$$v = \frac{RT_s}{h_{lv}}\left(C_2 - 0.5 - \frac{2 - q_C}{2q_C}\left(\frac{\gamma + 1}{2\gamma}\right)\left(\frac{c_p T_s}{h_{lv}}\right)\right) \tag{16}$$

where $\lambda_v$ is the vapor phase thermal conductivity, $Pr = \mu c_p / \lambda_v$ is the Prandtl number and $Kn$ is the Knudsen number, defined as the ratio between the droplet diameter and the molecular mean free path:

452

$$Kn = \frac{l}{2r_d} \qquad\qquad (17)$$

453

454  The two constants $C_1$ and $C_2$ in eq. ( 15 ) and ( 16 ) represents two tunable modelling parameters (see [18] for

455  a description of their significance) that are set respectively equal to 0.0 and 9.0, as suggested by Young [18].

456  Fig. 4 shows the comparison of the different model settings for four experimental cases (Exp. 252, 257, 193

457  and 411; for these last two measurements of the diameters are not available). Clearly, the use of the non-

458  isothermal correction significantly retards the nucleation process with respect to the isothermal case. In turn,

459  this results in a better agreement with experiments in all the simulated cases.

460  The adoption of the IAPWS correlation for the surface tension does not result in any detectable difference with

461  respect to the formulation proposed by Young [18]. This is because the difference in the surface tension as

462  predicted by the two correlations is always lower than 0.1% (at least for the range of temperature of interest

463  for this study). However, it is important to note that both these formulation describes the surface tension as a

464  function of the sole temperature and disregard any potential influence of the curvature radius.

465  Although it is generally acknowledged that the surface tension depends on the curvature for very small droplet

466  radii (especially below 10nm [28], which is the range of interest for wet steam flows), experimental evidences

467  are still required to specify how $\sigma$ depends on $r$ or even identify the sign of this variation (some studies suggest

468  that this may be temperature-dependent, with a transition from positive to negative upon increasing T above

469  ~250 K [28]). Moreover, due to its chief impact on the nucleation process ($\sigma$ appears within the exponential

470  term of eq. raised to the third power) any change in the expression for the surface tension most likely requires

471  a complete recalibration of the physical model settings and constants. As a result, most of the previous works

472  in the wet steam related literature have been accomplished exploiting the simplified flat-film surface tension

473  assumption, as in this study.

474  Finally, the most interesting comparison in Fig. 4 relates to influence of the droplet growth law. The analysis

475  of the various results reveals that the Young's droplet growth law can better capture the experimental trends

476  for the average radius. By contrast, the two laws appear to alternatively match the experimental trends for the

477  pressure, with the Young's law that always anticipate the nucleation region with respect to the Hill's

478  expression.

479  This fact can be explained by considering the specific calibration adopted for the Young's droplet growth law.

480  In particular, it is known that higher values of $C_2$ (as in this case) serve to boost the growth rate, resulting in

481  larger droplets whilst simultaneously shifting the pressure rise upstream [3]. The analysis of other boundary

482  conditions not reported here confirms the alternating performance of the two models. Therefore, it is not

483  possible at present to draw a definite conclusion as to which model performs the best and both these expressions

484  are tested for the analysis of the steam ejector.

485  Finally, it should be mentioned that the uncertainty connected to the pressure measurements was estimated by

486  Moses and Stein [8] to be about ±40 Pa (the corresponding error bars are approximately of the same size of

the experimental symbols in [Fig. 4](#)). In terms of droplet radius, Starzmann et al [3] make reference to an estimated uncertainty of perhaps ±20%, although the details of the derivation are not reported.
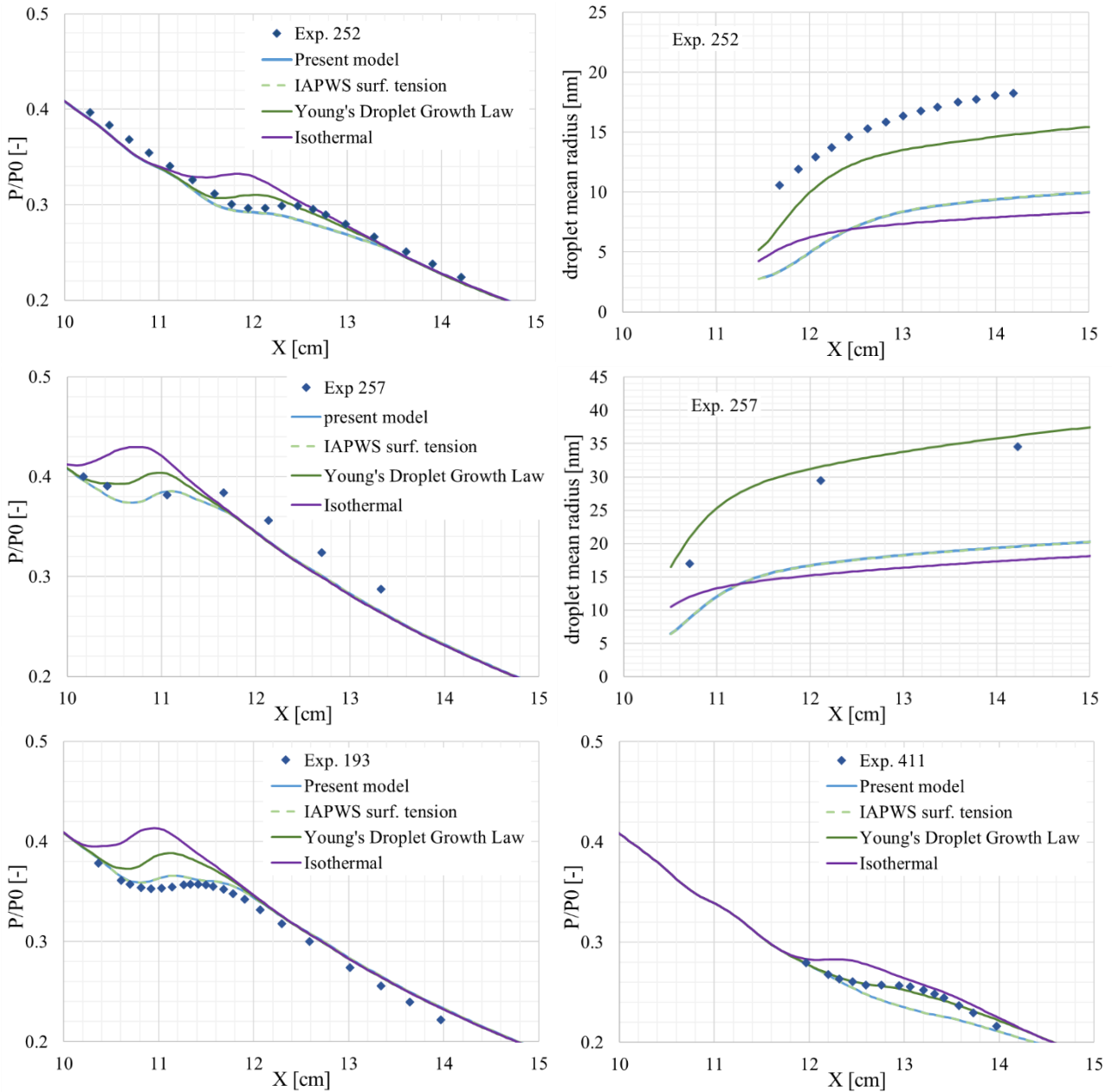


*Fig. 4 – Comparison of model settings for different cases: Exp. 252 ($P_0$=40050 Pa, $T_0$=374.3 K), Exp. 257 ($P_0$=67661 Pa, $T_0$=376.7 K), Exp. 193 ($P_0$=43023 Pa, $T_0$=366 K), Exp. 411 ($P_0$=42276 Pa, $T_0$=385.15 K)*

## 4. Steam Ejector

In this section, the developed model is validated against data from the supersonic steam ejector studied by Al-Doori [9] and Ariafar *et al* [5].

11

534  The set of boundary conditions analyzed are summarized in Table 1. The solution of the governing equations
535  is achieved exploiting a pressure-based coupled solver. A second order accurate up-wind scheme is selected
536  for the spatial discretization of all transport equations except for the volume fraction and momentum equations.
537  The first of these is discretized through a 3$^{rd}$ order QUICK scheme whereas for the latter a power-law scheme
538  had to be chosen due to numerical instabilities connected with the pressure-velocity coupling.
539  A k-ω SST turbulence model is selected for all the simulations because of the specific calibration for transonic
540  applications [29] and based on previous studies on single phase ejector flows [30] [31]. In addition, due to the
541  high Mach reached within the ejector mixing chamber, two additional UDFs are built to endow the turbulence
542
543  *Table 1: Summary of ejector boundary conditions*

| Stream | Total Temperature [K] | Total Pressure [kPa] |
|---|---|---|
| Motive | 403 | 270 |
| Suction | 287 | 1.6 |
| Discharge | | From 4.2 to 7.5 static pressure |

544
545  model equations with the correction for compressible mixing layer (in ANSYS Fluent, these are available only
546  for single-phase flows).
547  Fig. 5 shows the computational domain used for all the CFD analyses. Due to the high directionality of the
548  flow (axial velocity component always greater than transversal component), a structured grid is selected to
549  reduce numerical diffusion. Moreover, a straight channel is added at the end of the domain, due to the presence
550  of large recirculation regions at the ejector outlet that prevented reaching stable convergence for some
551  operating conditions. Although this change may induce some approximations, these are most probably limited
552  to a small region near the outlet (the flow upstream of the shock in the diffuser is not influenced due to the
553  hyperbolic nature of the supersonic flow). Moreover, the inclusion of the channel prevents backflow of
554  unknown characteristics from entering into the ejector and allows the recirculation to reattach within the
555  computational domain, thus improving the numerical stability of the simulations.
556  The adequacy of the mesh refinement was checked by comparing the mass flow rates results for three different
557  grids having all y+ values less than 1 along the ejector surfaces. Table 2 shows the results of the study. In order
558  to reduce the computational time, the grid with 70k quadrilateral cells is selected for all subsequent
559  calculations.
560  Convergence of the solution is defined by an error in the mass flow imbalance of less than $10^{-5}$ kg s$^{-1}$ and
561  calculations are stopped when all residuals are stable. Walls are assumed to be adiabatic and smooth.
562
563
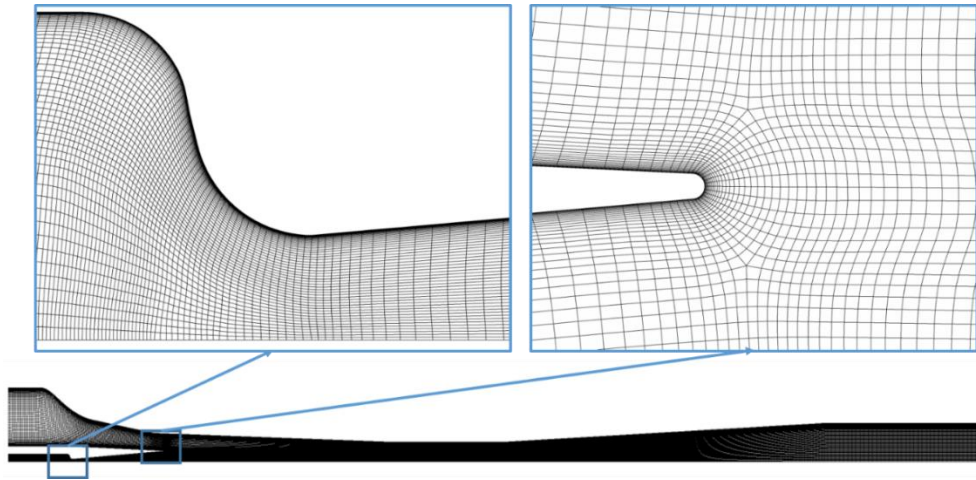
Fig. 5 – Computational domain and mesh details of the primary nozzle throat and fillet (grid with 70k cells)

*Table 2: Grid independence study*

| Grid cells | Mass flow rate [kg/s] | | | Difference with finer mesh | | |
|---|---|---|---|---|---|---|
| | Motive | Suction | ER | Motive | Suction | ER |
| ~35 000 | 0.00341 | 0.00111 | 0.327 | 0.5% | -13.0% | -13.4% |
| ~70 000 | 0.00339 | 0.00128 | 0.377 | 0.1% | 1.2% | 1.1% |
| ~140 000 | 0.00338 | 0.00126 | 0.373 | - | - | - |

*Entrainment Ratio and mass flow rates*

Fig. 6 shows the comparison between the experimental and numerical Entrainment Ratio (ER) curves. Both the Young's and Hill's droplet growth law are tested (hereafter referred as Yg82 and Hi66). Details of the experimental apparatus and measurement procedures can be found in [9] (chapter 4 and 5). According to Al-Doori [9] the uncertainty level for the ER is around ±3%. The numerical simulations produce a higher value of ER at on design with a percent difference of about 14%. Moreover, CFD models somewhat anticipate and smoothen the transition toward the off design regime.

Despite the large discrepancy, Fig. 7 illustrates that when results for the motive and suction flows are analyzed separately, differences are smaller than the corresponding value of ER. This is due to a summation of the errors when dividing the two quantities (in other studies, the authors have found that the discrepancy was lower for the ER than the mass flow rates, as in [30]). In particular, the greatest discrepancy is achieved for the data of the suction flow rates, with a percent difference of about 7% at on design, whereas the difference for the motive flow rate is slightly less than 6%. For these two quantities, Al-Doori [9] reports uncertainties of 0.6% and 1-2% for the primary and secondary mass flow rate, respectively.

In terms of models sensitivity, the change of the droplet growth law seems to have a limited influence on the ejector mass flow rates. The only minor change occurs at off design, where the Hill's model performs slightly better than the Young's law. Moreover, a check of many flow variables has revealed only minor differences between the two models, as illustrated in Fig. 8 for the volume fraction and Mach profile along the ejector
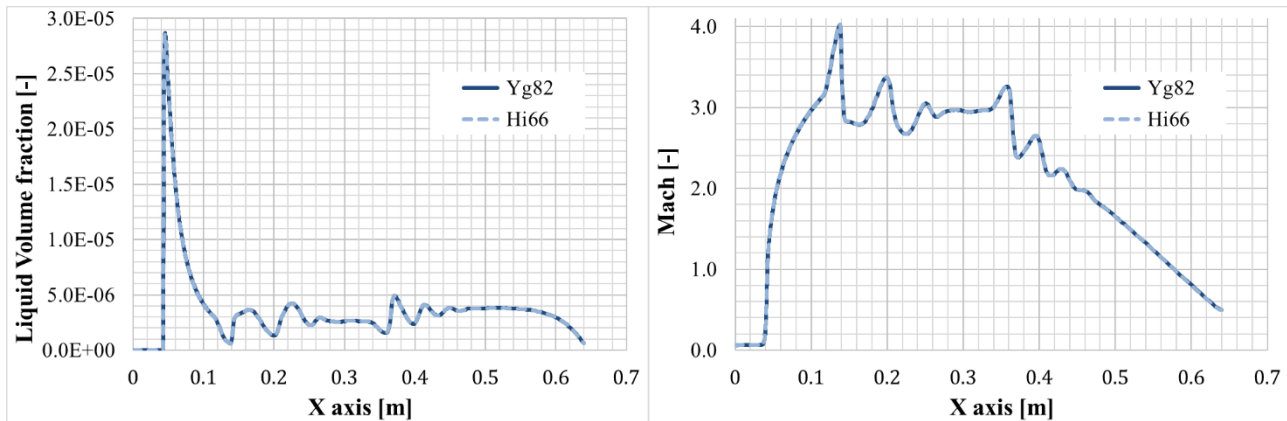
616   axis. Consequently, all the subsequent analyses in this paper are carried out by considering only the Hill's
617   droplet growth expression.

618
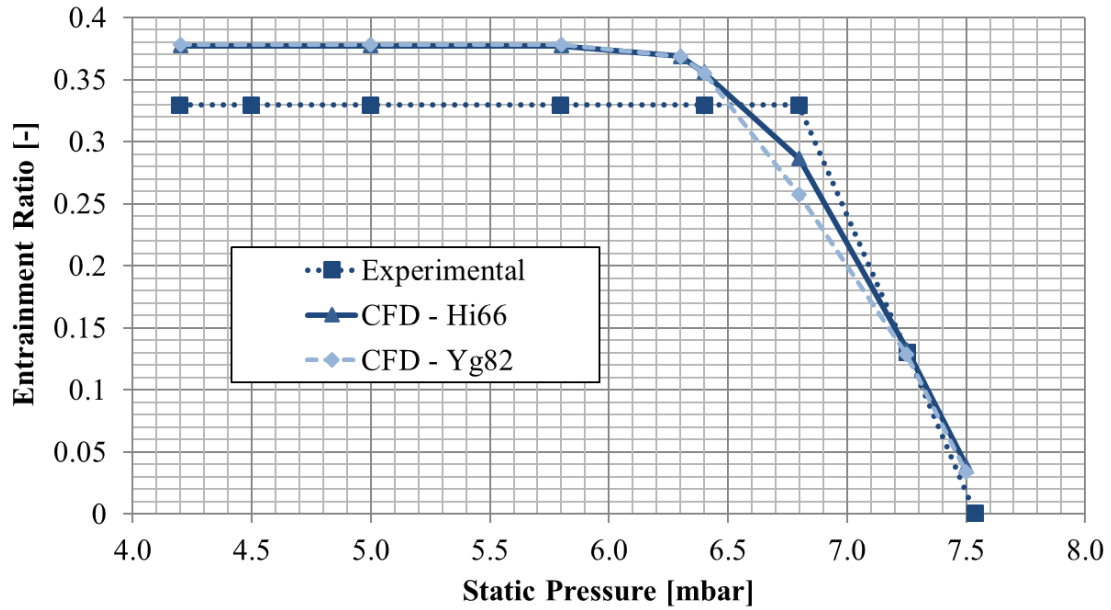


619

620   *Fig. 6 – Comparison of experimental and numerical ER (experimental data are taken from [9])*

621
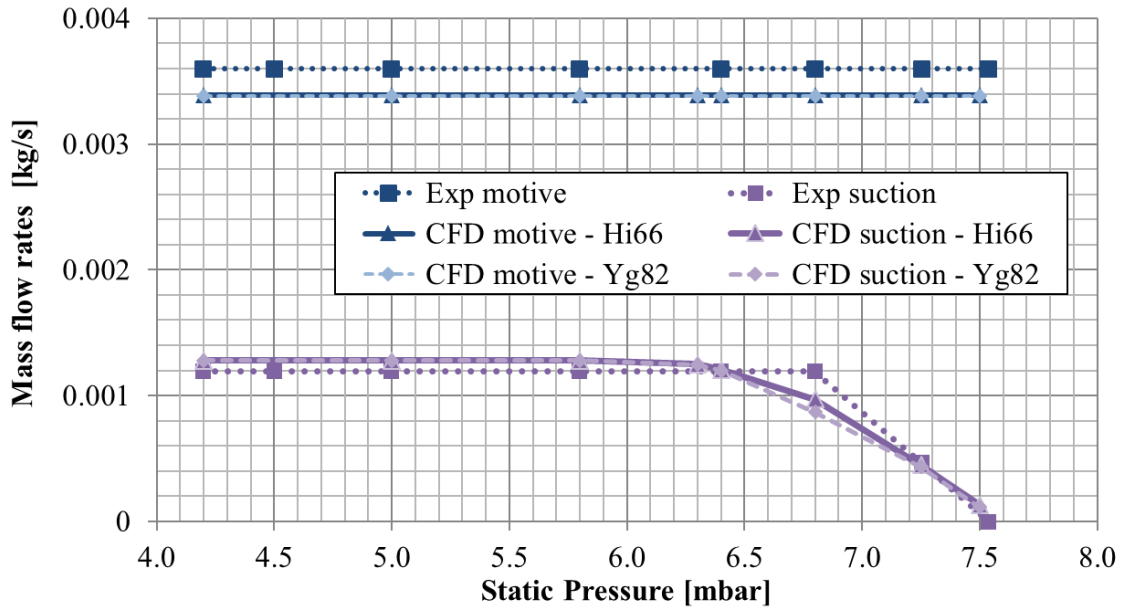


622

623   *Fig. 7 – Comparison of experimental and numerical mass flow rates (experimental data are taken from [9])*

624

*Fig. 8 – Liquid Volume Fraction (left) and Mach Number (right) profiles along the ejector axis. Comparison of different droplet growth models ($P_{out}$ = 4.2 kPa)*

### Accuracy of mass flow rates predictions

Despite the general trend for ER being well reproduced, the discrepancy on the primary flow rate is still large compared with the error that should reasonably arise from the simulation of the 1D flow across a De Laval nozzle. A first possible cause for this discrepancy may come from numerical inaccuracies due to the low grid refinement and low order discretization (especially for the momentum equation). In order to check this hypothesis, a grid/order independence was performed solely on primary nozzle and the results are shown in Table 3. Clearly, despite some differences between the low and high order schemes remaining even for the finest mesh, the scatter is in all cases well below the 1%.

One further reason for the discrepancy of the primary flow rate may be the presence of liquid at motive inlet (it should be noted that no superheating was imposed in the experimental tests). This may increase the average density of the stream passing through the throat, producing a larger value of experimental flow rate. Moreover, the presence of liquid nuclei or steam impurities (such as solid particles) may strongly affect the intensity and type of the condensation process (see for instance [12]). In this respect, a sensitivity analysis was performed by varying the amount of liquid mass fraction at nozzle inlet (the simulations were performed for the 22k nozzle mesh with the 3 order accurate scheme). The results of these trials showed that in order to increase the motive mass flow rate of about 6%, it is necessary to impose nearly 15% of liquid mass fraction at inlet[1], which is a too large amount to explain the discrepancy with experiments. Nevertheless, these trials were performed with the single-fluid approach described previously. This method is generally not suited to investigate problems with secondary or multiple nucleation [32]; hence, the obtained results cannot exclude the presence of liquid nuclei at the motive inlet, which could have an impact on the experimental trends.

Finally, one further cause may be the uncertainty connected with the experimental measurements and with the geometrical dimension of the throat. As for the first, Al-Doori [9] estimates an uncertainty of around 0.6% for the primary mass flow rate, which is almost one order of magnitude lower than the differences with CFD. On

---

[1] This indicates that change in flow rate does not linearly depend on density variations, for instance, adding 6% percent of mass fraction at inlet leads to an increase of around 1.5% of the primary flow rate

680  the other hand, previous studies performed on a single phase air ejector [30] have shown that even small

681  uncertainties in the throat dimension (connected mostly with the manufacturing process), can lead to

682  discrepancies in the mass flow rate up to many percents. Unfortunately, Al-Doori does not report information

683  on the geometrical uncertainty and manufacturing precision for the investigated profiles. Nevertheless, a first

684  estimation of the sensitivity to the nozzle throat diameter can be achieved by making use of the compressible

685  1D equations for perfect gases.

686  By considering an average specific heat ratio of 1.3 (as found from inspection of CFD results), this method

687  returns a primary mass flow rate ~ 0.00336 kg/s, which is around 1% lower than CFD results. By making use

688  of this simple approach, it is found that an increase of only 16 μm (i.e., 1% of the nominal diameter) produce

689  a change of the mass flow rate of more than 2%. If we consider this estimated sensitivity to approximately

690  hold for CFD simulations, it follows that a discrepancy of around 50 μm may provide a difference close to the

691  one obtained in the present simulations.

692  It is concluded that both the presence of liquid at inlet and possible geometrical uncertainties may have played

693  a role in the observed differences with experimental primary flow rate.

694

695  *Table 3: Motive nozzle mass flow rates for different grid size and discretization schemes*

| Discr. order<br>Grid size | 1st order | Present setup | Full 2nd order | 3rd order |
|---|---|---|---|---|
| ~22 000* | 3.388 E-03 | 3.388 E-03 | 3.369 E-03 | 3.371 E-03 |
| ~44 000 | 3.376 E-03 | 3.378 E-03 | 3.363 E-03 | 3.365 E-03 |
| ~88 000 | 3.376 E-03 | 3.376 E-03 | 3.357 E-03 | 3.357 E-03 |

696  *this is the mesh size used for the ejector calculations

697

698  We focus now on the suction flow rate. From a general viewpoint, it is known that accurate predictions of the

699  entrainment process requires accounting the influence of compressibility on the mixing layer. In particular,

700  experimental investigations performed in the 70s (e.g., [33] [34]) have shown that compressible mixing layers

701  are affected by a significant reduction of the spreading rate with respect to equivalent low-speed

702  configurations.

703  Although this effect has been known for a long time, no convincing theoretical explanation has been given yet

704  and turbulence models predict this decrease empirically (see Smits and Dussauge [35] or Gatsky and Bonnet

705  [36] for more details). For ω-based models, Wilcox [37] proposes a correction to the turbulence kinetic energy

706  equation based on the turbulent Mach number:

707

$$Ma_t = \frac{\sqrt{2k}}{a} \qquad (18)$$

708

709  where $k$ is the turbulent kinetic energy and $a$ is the speed of sound.

710  The compressibility correction reduces the mixing layer entrainment by increasing the dissipation of

711  turbulence kinetic energy within shear layers. Although its use improves the accuracy for compressible mixing

16

741 layers, the correction can negatively affect predictions for wall boundary layers at transonic and supersonic
742 speeds [38]. Because of this, the application of the correction was carefully evaluated.

743 Fig. 9 shows a comparison of the turbulent Mach number field between a simulation with the compressibility
744 correction active and one without correction. As can be seen, the turbulent Mach reaches very high levels
745 within the mixing layer and downstream of the shock in the diffuser. In particular, a substantial part of the
746 mixing layer presents values of $Ma_t$ larger than 0.25, which is the threshold for compressibility to have any
747 impact on the mixing layer [38]. The use of the correction limits these peak values and reduces the mixing
748 layer spreading rate. In turn, the suppression of the spreading rate results in a reduction of the suction flow rate
749 of nearly 17% percent. Therefore, the difference with the experimental mass flow rate would be of about 22%
750 without the compressibility correction (as opposed to the 7% obtained with the correction).

751
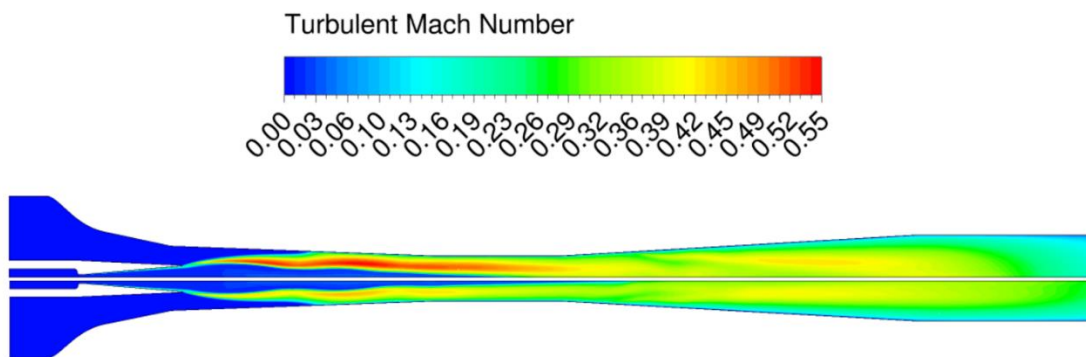
752


753 *Fig. 9 – Turbulent Mach number contour for the case with compressibility correction (bottom) and without*
754 *compressibility correction (top) ($P_{out}$ = 4.2 kPa)*

755

756 ***Wall Pressure Profile***

757 Fig. 10 presents the results for the pressure profiles along the ejector wall. In order to perform the comparison,
758 the outlet boundary conditions were imposed so as to match the value of the last pressure probe in the diffuser.
759 This was necessary due to the presence of large recirculations along the diffuser that prevented the pressure
760 recovery from completing at the ejector outlet (it should be noted that the straight channel attached downstream
761 of the diffuser begins at *x= 535.5 mm*).
762 Overall, the comparison with experimental data shows a good agreement, especially near the mixing chamber
763 entrance and throat regions. The accord with experiments decreases as flow approaches the diffuser, where the
764 recirculations are found. These are notoriously hard to capture by common two-equation turbulence models
765 and could partly account for the differences with experiments. Furthermore, the discrepancies in the prediction
766 of the mass flow rates may also impact the results for the pressure trends. This is because the energy budget of
767 the total stream is altered due to the different proportions of motive and suction flows, changing the positions
768 of the shock within the diffuser as well as the pressure recovery trends.

769

17
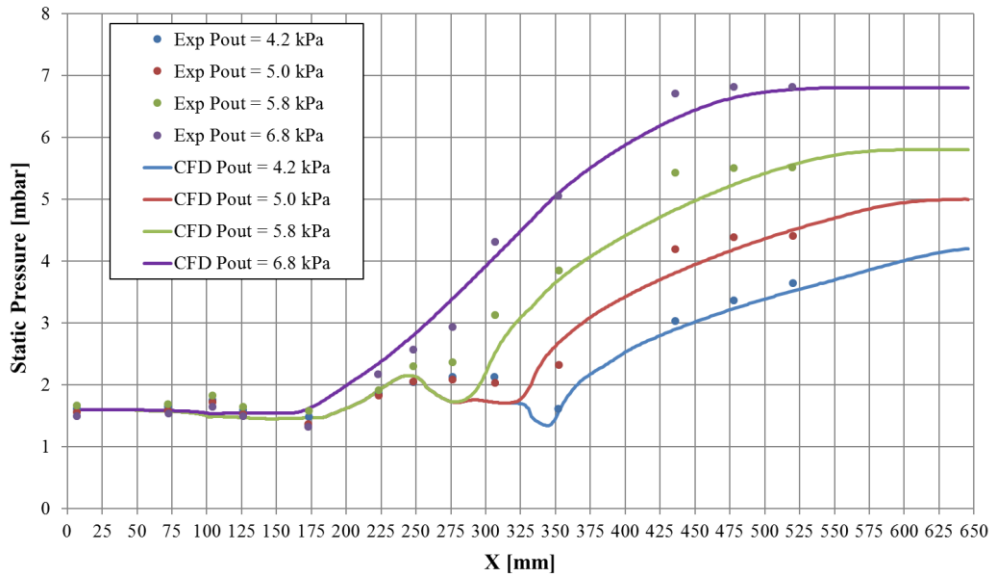
788
789    *Fig. 10 – Comparison of experimental and numerical wall pressure profiles (experimental data are taken*
790    *from [9])*
791
792    Fig. 11 and Fig. 12 show the flow recirculation patterns and shock train structures for the different outlet
793    pressures. It is interesting to note that the case with the lowest outlet pressure present a flow pattern that consists
794    of two different vortex structures. A first one, smaller, occurs right after the shock train in the diffuser, and a
795    second, larger, farther downstream. This case also presents the best agreement with the experimental pressure
796    trend. According to CFD, the patterns adjust to a single vortex structure when the outlet pressure is increased.
797    However, the agreement with experiments is reduced, therefore, these numerical patterns should be considered
798    with some caution. Finally, the numerical Schlieren contours in Fig. 12 show that the pressure-based scheme
799    adopted in this work can qualitatively reproduce the shock train structures within the ejector. However, the
800    thickness of each shock may be overestimated due to the higher numerical diffusion of these schemes.
801
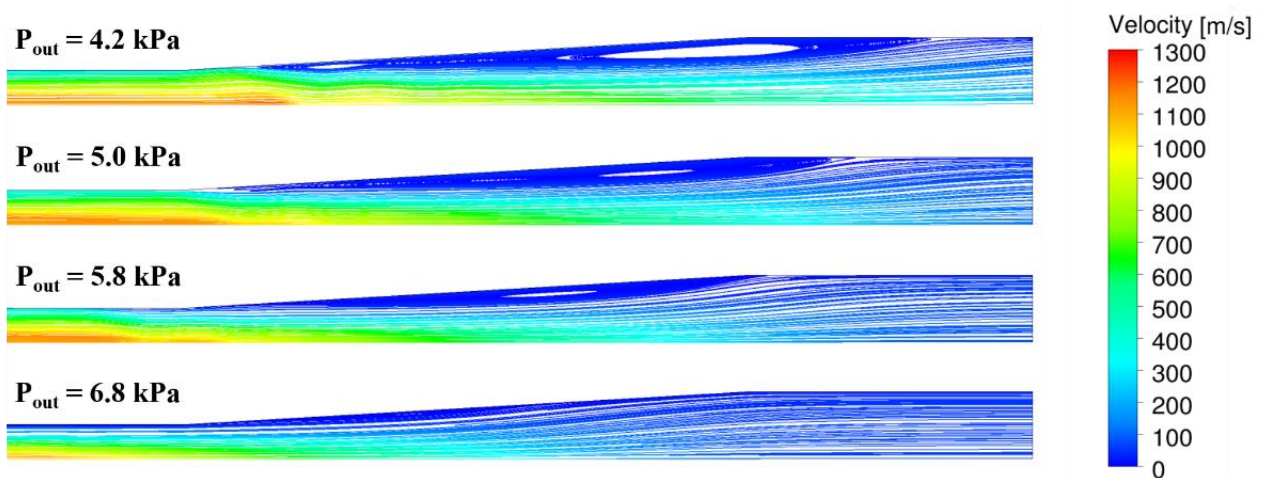


802
803    *Fig. 11 – Streamline pattern at the ejector outlet showing the recirculation regions*
804
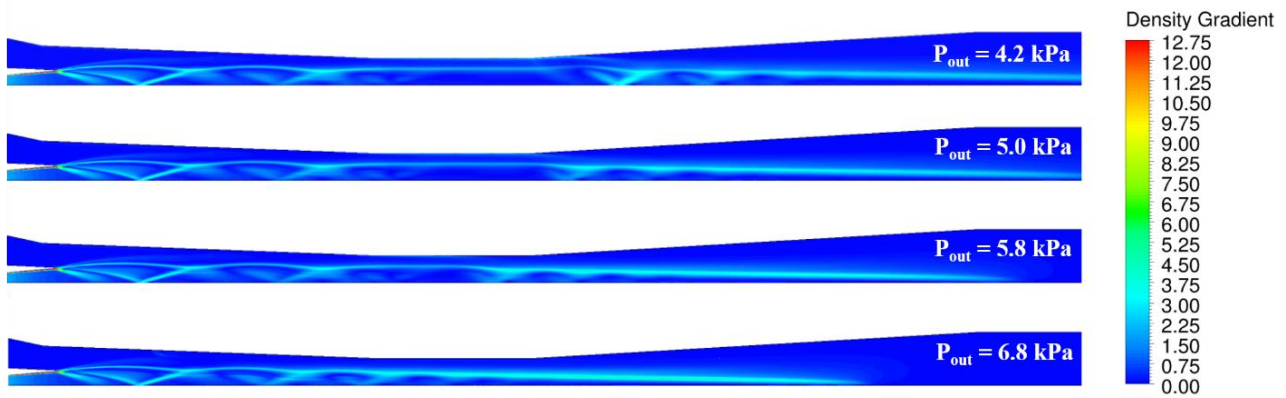
Fig. 12 – Numerical Schlieren images (density gradient contours) showing the shock train structures

### Two-phase flow features

Fig. 13 shows the contour of the liquid mass fraction for the case with the lowest outlet pressure ($P_{out}$ = 4.2 kPa). As can be seen, the condensed phase reaches value up to 20% of the total mass, with peak levels in the region downstream of the nozzle exit plane. This is due to the further acceleration caused by the primary jet under-expansion. The absence of any superheating of the motive stream exacerbate this problem that can lead, in some extreme cases, to the formation of ice inside the ejector (as discussed in the next section).

Fig. 13 further illustrates that the liquid mass fraction evaporates almost completely toward the ejector outlet, where the mixed stream undergoes the shock trains and decelerate to reach the outlet pressure. In addition, the liquid mass fraction goes to zero at the nozzle wall, due to the heat recovery caused by the fluid deceleration and viscous dissipation within the boundary layer [1].
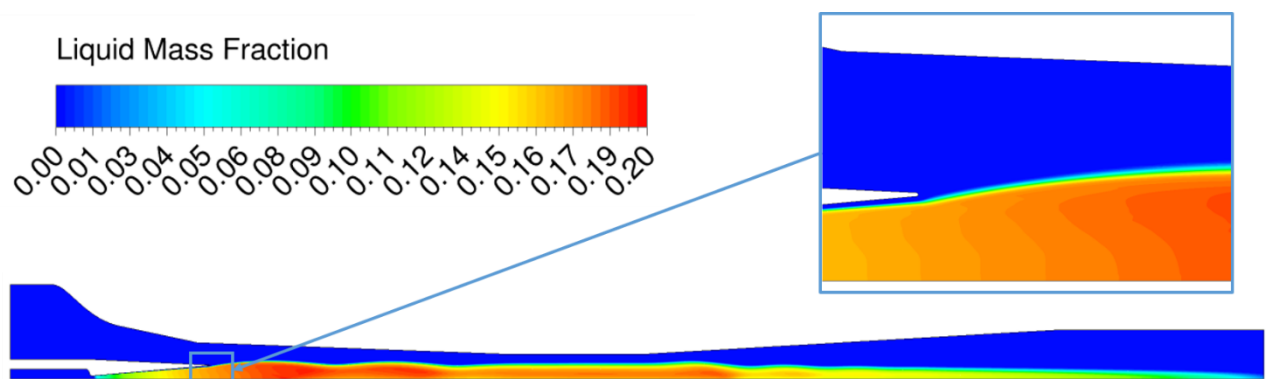


Fig. 13 – Liquid mass fraction contour (case with $P_{out}$ = 4.2 kPa)

Fig. 14 shows the contour of the droplet number per unit mass of mixture, $n$. The figure displays also the line representing the boundary where the liquid mass fraction is zero.

The contour clearly reveals the presence of a radial distribution of the droplet number. This stems from the significant curvature of the nozzle profile at the throat, which induces a region of low pressure near the wall

19

880     and causes a stronger nucleation. The nucleated droplets are then convected down the ejector along streamlines

881     and the radial distribution persist almost unaltered till the outlet.

882     The analysis of Fig. 14 further shows that the droplets number contour follows closely that of the liquid mass

883     fraction depicted in Fig. 13. This is a direct consequence of the assumption of equal velocity between the

884     phases. Yet, the comparison reveals also that toward the ejector outlet, where the condensed mass evaporates

885     completely, the liquid droplets do not disappear but survive in the form of nuclei with zero mass and volume.

886     The reason for this numerical error is to be found in the absence of a "droplets sink" term within the droplet

887     transport equation, eq. ( 5 ).

888     This is a common feature of the single-fluid approaches which partly prevent their use in applications where

889     secondary nucleation occurs (e.g., multi-stage steam turbine cascades). Although in principle it could be

890     possible to add a sink term to the droplet number equation, in practice, the differential nature of the droplet

891     transport equation complicates this task. For instance, the inclusion of a negative sink term in eq. ( 5 ) leads to

892     regions with negative numbers of droplets. This problem may be worked around by positively limiting the

893     value of the droplet number. Unfortunately, this is not possible in ANSYS Fluent.

894     Other options may exist in which, for instance, the value of the sink term is related to the number of droplets

895     existing in the cell or it is described on a logarithmic basis. To the authors' knowledge, these approaches have

896     never been attempted before and may require an extensive development work. However, this effort may not

897     be completely justified in view of the fact that the assumptions implicit in the single-fluid approach would

898     anyhow lead to significant approximations (e.g., the droplet sizes originating from different nucleation sites

899     are averaged out). In this respect, the adoption of more advanced schemes, such as the multi-fluid approach

900     mentioned in the introduction or a Lagrangian approach (e.g., [32]), naturally account for the removal of

901     droplets from the computational domain and can provide more accurate results than the method used in this

902     work.

903
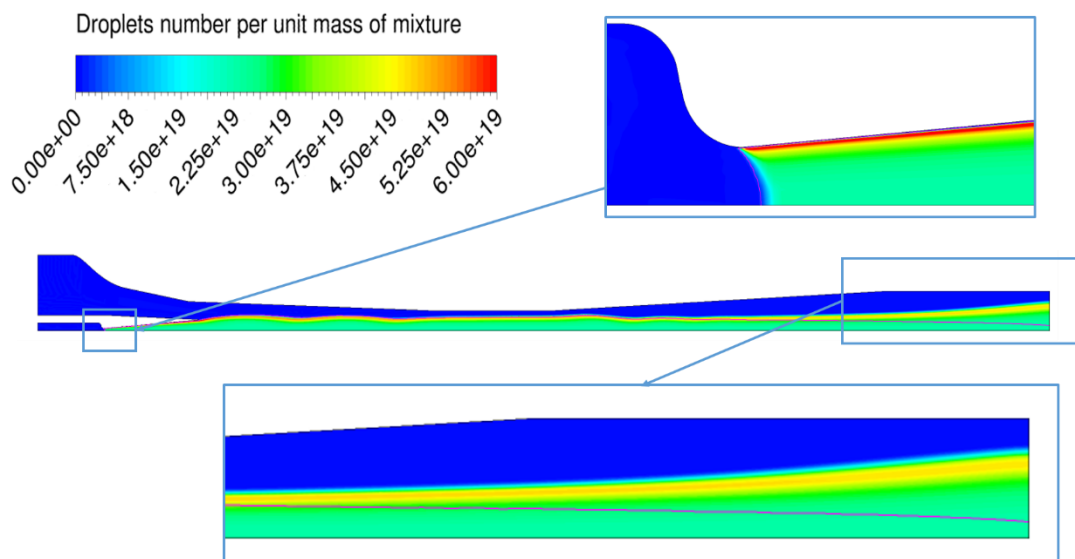


904

905     *Fig. 14 – Contour of the droplet number per unit mass of mixture (in purple is the line where the liquid mass*

906     *fraction is zero; case with $P_{out}$ = 4.2 kPa)*

*Model limits*

In this final section, we would like to review certain specific limits connected with the developed model and discuss possible implications deriving from them. In doing so, we focus on those assumptions that seem particularly restrictive with respect to steam ejector applications.

A first limit connected with the developed model relates with the droplet growth regime. Generally speaking, the growth rate formulation for a liquid droplet is calculated differently depending on value of the Knudsen number. During the initial phase of the droplet growth, the liquid nucleus is generally much smaller than the mean free path, i.e., *Kn>>1*. Under these conditions, named as *free molecular regime*, the continuum hypothesis does not hold and the calculation of the droplet growth must be accomplished by means of kinetic theory or statistical mechanics concepts. At the other extreme is the situation where *Kn<<1*. In this case the droplet is large enough to apply the macroscopic balances for heat, mass and momentum. In between these two conditions is what is called the transition regime (*Kn~1*). This is the most difficult to analyze and is usually handled by means of interpolations formulae that connect the continuum and free molecular regimes (see for example [18]).

Specifically, the Hill's droplet growth law adopted in this work is valid only for the free molecular regime, so that some questions may arise about its applicability to ejector flows (especially in the case of under-expanded nozzles with a delayed appearance of shocks that can vaporize or reduce the droplet dimensions [1]).

Fig. 15 shows the trend of the Knudsen number along the ejector axis, for one of the simulated cases (but all cases present similar trends). Clearly, the value of Kn is always well above unity except for a very small region near the primary nozzle throat. In this zone, the vapor temperature is still high and the mean free path is of the same order of magnitude of the droplet diameters (around $10^{-9}$ m).
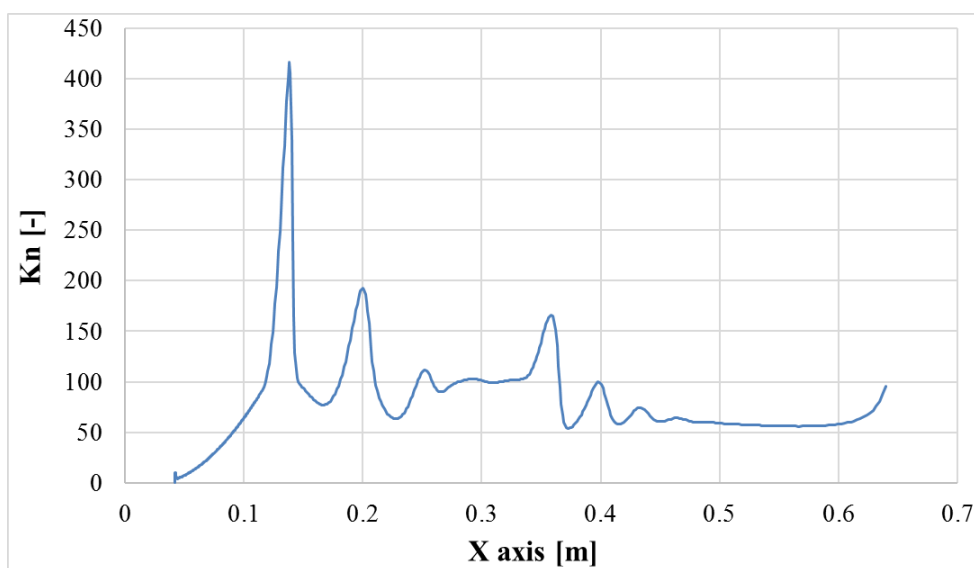


*Fig. 15 – Knudsen number trend along the ejector axis (case with $P_{out}$ = 4.2 kPa)*

994 Somewhat connected with the issue of the droplet growth regime is the assumption of velocity equilibrium
995 between the phases. In order to understand whether a particle will follow the gaseous stream trajectory or
996 depart from it, it is possible to estimate the Stokes number related with the particle velocity [39].
997 The Stokes number is defined as the ratio between the droplet response time to a variation in the velocity field
998 and a flow characteristic time of the continuous phase:
999

$$St = \frac{t_d}{t_v} \qquad (19)$$

1000

1001 When the Stokes number is much lower than unity, the condensed phase will closely follow the gaseous stream
1002 and it is allowed to assume a common velocity between the phases, as in the present work.
1003 The droplet response time depends on the condensed phase inertia and on the carrier phase viscosity [39]:
1004

$$t_d = \frac{\rho_d D_d^2}{18\mu_v} \qquad (20)$$

1005

1006 The carrier phase time can be calculated as the ratio between a characteristic velocity and length scale:
1007

$$t_v = \frac{u_v}{L} \qquad (21)$$

1008

1009 Clearly, the definition of this last quantity is somewhat arbitrary because no specific definition of the
1010 characteristic length is provided. For nozzle flow, this is often the throat diameter, the use of which would give
1011 an estimate of St ~$10^{-3}$. However, this result refers to a characteristic time representative of the mean flow and
1012 does not consider any possible velocity mismatch arising from the interaction between turbulence and the
1013 dispersed phase. To this aim, $t_v$ can be chosen so as to represent a turbulent characteristic time. Specifically, it
1014 is possible to calculate the Stokes number by using the inverse of the specific dissipation rate, which represents
1015 the frequency of the smallest turbulent eddies (those occurring at the Kolmogorov scale), i.e.:
1016

$$t_v = t_{turb\_min} = \frac{1}{\omega} \qquad (22)$$

1017

1018 where $\omega$ is the specific dissipation rate.
1019 Fig. 16 shows a map of this "turbulent" Stokes number within the ejector. Clearly, the assumption of
1020 equilibrium velocity appears to be satisfied in the whole two-phase flow domain, meaning that the fluid particle
1021 velocity should follow not only the average flow trajectories, but also the path of the smallest turbulent eddies
1022 (those with the highest frequency).
1023 However, it should be noted that the above Stokes number was calculated under the assumption of "smooth"
1024 flow conditions. The presence of any local perturbation may notably reduce the characteristic length, which,

in the specific case of a dynamic shock, is generally of the same order of magnitude of the molecular mean free path. In this case, the different inertia between vapor and liquid droplets may produce a local velocity mismatch and lead to the departure of the phase trajectories. Moreover, the effects of drag and interphase momentum exchange has been neglected in this work although it could represent a non-negligible source of kinetic energy losses. Detailed analyses of these type of processes is a complex task and may require the use of more advanced models than the single-fluid approach.
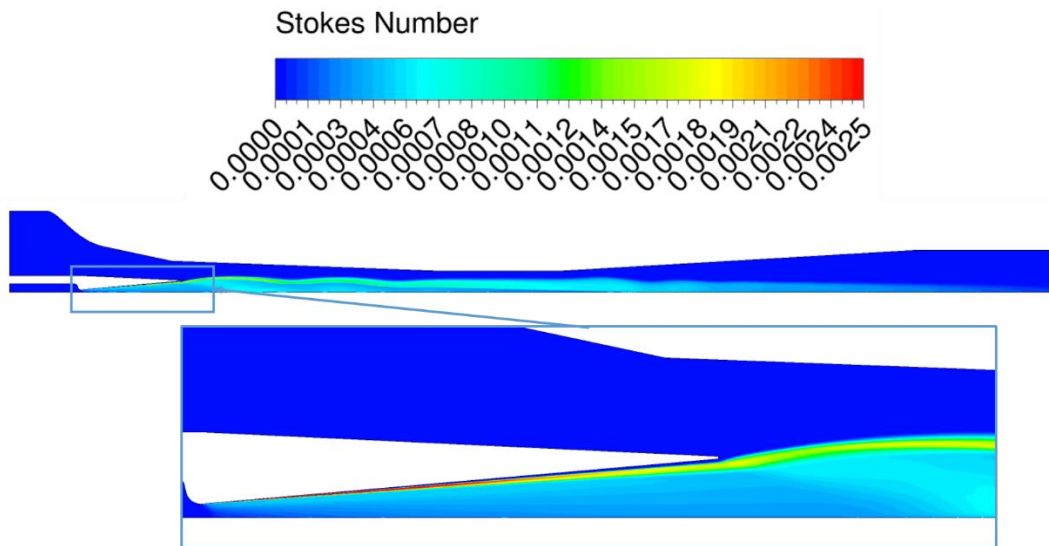


*Fig. 16 – "Turbulent" Stokes number within the ejector (case with $P_{out} = 4.2$ kPa)*

Finally, a last, key aspect that is of particular concern for steam ejector studies is related to the very low temperature levels attained by the expanding stream. This problem is particularly critical for ejector refrigeration applications, where efficiency considerations impose the use of low or no level of superheating at the inlet of the motive stream (this is also the case for the experimental results used in this work). Consequently, the motive jet can reach temperature levels that go well below the triple point, causing the possible appearance of ice.

Fig. 17 shows the mixture temperature contour within the ejector. Clearly, the temperature goes well below the limit of the triple point and the presence of ice cannot be excluded (especially downstream of the nozzle exit plane where the mixture temperature reaches values close to 210 K). Nevertheless, ice crystal formation, in much the same way as for droplet nucleation, is fundamentally a time dependent phenomenon and some degrees of supercooling usually exists before the water vapor or liquid starts to solidify.

In particular, experiments in cloud chambers with pure water vapor indicates that the homogeneous nucleation of ice usually occurs with around 30-40 K of supercooling [40]. By contrast, recent investigations in supersonic nozzles have shown that for the high cooling rates and small cluster sizes that are achieved in these devices, the supercooling can be as high as 90 K (i.e., supercooled water temperatures of nearly 190 K) [41]. However, these tests were conducted with ultrapure water and may not be directly applicable to the present study (this is

1079     because impurities in the water droplets or vapor stream can greatly anticipate crystal formation). As a result,

1080     the presence of ice cannot be excluded in the steam ejector under investigation.

1081     The appearance of water ice crystal may induce substantial modifications to the mixture flow behavior. For

1082     instance, the change in the latent heat release (from the value of condensation to that of solidification) may

1083     modify the nozzle Mach and pressure profiles. Moreover, phenomena such as crystals agglomeration and

1084     deposition may be important and could lead to modifications in the ejector geometrical profiles. On the other

1085     hand, the presence of shocks immediately after every steam expansion may lead to the sudden melting of the

1086     ice, limiting its impact on the global flow dynamics. In this case, numerical simulations may still incur in

1087     significant discrepancies due to the uncertain extrapolation of the supercooled water properties below the triple

1088     point temperature (most of these, including viscosity, specific heat, surface tension and others, present

1089     exponential variations with decreasing temperatures [40]). In view of these many aspects, it is important that

1090     future experimental investigations properly address the analysis of ice formation inside steam ejectors.

1091
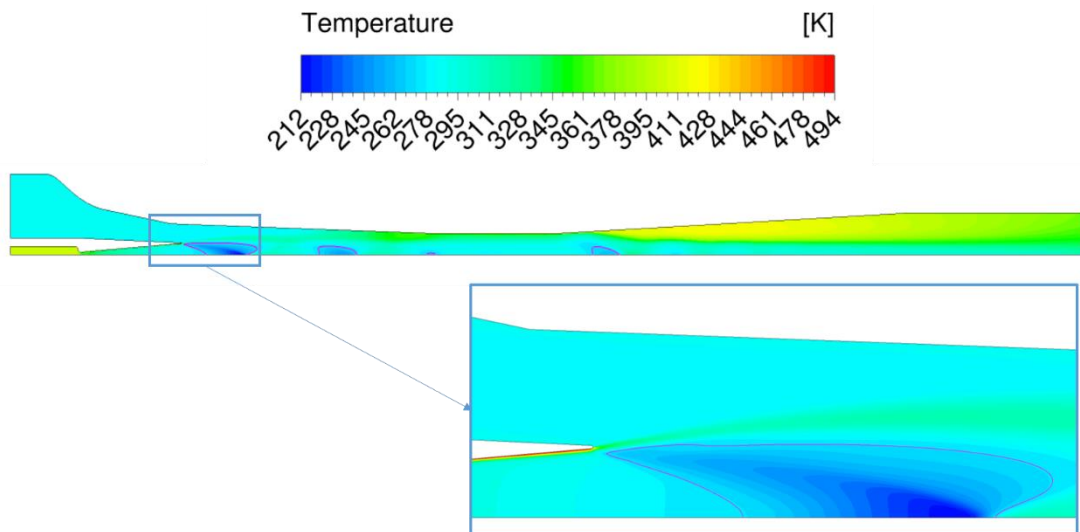


1092

1093     *Fig. 17 – Temperature trend along the ejector; in purple is the line corresponding to the triple point*

1094     *temperature  (case with $P_{out} = 4.2$ kPa)*

## 5. Concluding remarks

1096     A numerical model for the simulation of wet-steam flow has been developed and implemented within the CFD

1097     software ANSYS Fluent via User Defined Functions. This approach allows great flexibility in the choice of

1098     the physical model settings and calibration parameters.

1099     The model has been tested against experimental data from a De-Laval nozzle and a steam ejector test-case.

1100     The nozzle simulations have shown that the developed model can produce results that substantially agree with

1101     experiments and that are in line with those provided by the ANSYS Fluent wet steam model. However, the

1102     model improves on the Fluent built-in scheme by providing a proper conservation of the number of droplets

1103     within the computational domain. The analysis of the sensitivity to changes in model settings has shown the

1104     importance of both the nucleation rate non-isothermal correction and droplet growth law in predicting the

24

1105 condensation starting position. By contrast, the adoption of the IAPWS correlation for the surface tension did

1106 not result in any detectable difference with respect to the formulation used in the present model.

1107 Simulations for the steam ejector test case have demonstrated a substantial agreement with experiments, both

1108 in terms of mass flow rates and wall pressure profiles. Some discrepancies are found for the primary mass flow

1109 rate that probably stems from the presence of liquid at the nozzle inlet or from uncertainties in the nozzle throat

1110 dimensions. The entrainment of the secondary flow can also be reproduced with accuracy, as long as the effects

1111 of compressibility on mixing layer development are accounted for in the turbulence model.

1112 The analysis of the internal flow features has shown that, due to high level of expansion of the primary jet, the

1113 liquid mass fraction reaches values up to 20% within the mixing chamber. In this region, the mixture

1114 temperature goes well below the water triple point, indicating the possible presence of ice. However, the

1115 limited residence time and the presence of shocks may limit the impact of ice formation on the flow dynamics.

1116 The assessment of the Knudsen and Stokes numbers within the ejector suggests that the approximations of free

1117 molecular droplet growth regime and velocity equilibrium between the phases should be valid, at least in the

1118 flow regions away from dynamic shocks.

1119 In conclusion, it is important to note that some of the most important limitations of the model are related to the

1120 assumption of the flat-film surface tension as well as to the absence of a sink term in the droplets number

1121 equation. Improvements in both these two aspects may greatly increase the prediction capability of the wet-

1122 steam model but require an extensive development and tuning process that will be the subject of future studies.

1123

# References

1125

[1] P. P. Wegener and L. M. Mack, "Condensation in Supersonic Wind Tunnels," in *Advances in Apllied Mechanics*, New York, Academic Press Inc., 1958, pp. 307-440.

[2] P. G. Hill, "Condensation of water vapour during supersonic expansion in nozzles," *J. Fluid Mech.,* vol. 25, no. 3, pp. 593-620, 1966.

[3] J. Starzmann, F. R. Huges, A. J. White, J. Halama, V. Hric, M. Kolovratnik, H. Lee, L. Sova, M. Statny, S. Schuster, M. Grubel, M. Schatz, D. M. Vogt, P. Y., G. Patel, T. Turunen-Saaresti, V. Gribin, V. Tishchenko, I. Garilov and e. al., "Results of the International Wet Steam Modelling Project," Prague, 2016.

[4] T. Sriveerakul, S. Aphornratana and K. Chunnanond, "Performance prediction of steam ejector using computational fluid: Part 1. Validation of the CFD results," *International Journal of Thermal Sciences,* vol. 46, pp. 812-822, 2007.

[5] K. Ariafar, D. Buttsworth and G. Al-Doori, "Effect of mixing on the performance of wet steam ejectors," *Energy,* vol. 93, pp. 2030-2041, 2015.

[6] X. Wang, L. H.J., D. J.L. and T. J.Y., "The spontaneously condensing phenomena in a steam-jet pump and its influence," *International Journal of Heat and Mass Transfer,* vol. 55, p. 4682–4687, 2012.

[7] K. Chunnanond and S. Aphornratana, "An experimental investigation of a steam ejector," *Applied Thermal Engineering,* vol. 24, pp. 311-322, 2004.

[8] C. A. Moses and G. D. Stein, "On the growth of steam droplets formed in a Laval nozzle using both static pressure and light scattering measurements," *Journal of Fluids Engineering,* pp. 311-322, 1978.

[9] G. Al-Doori, Investigation of Refrigeration System Steam Ejector Performance Through Experiments and Computational Simulations, Ph.D. thesis, University of Southern Queensland, 2013.

[10] F. Giacomelli, G. Biferi, F. Mazzelli and A. Milazzo, "CFD modeling of supersonic condensation inside a steam ejector," *Energy Procedia,* no. 101, pp. 1224-1231, 2016.

[11] A. Gerber and M. Kermani, "A pressure based Eulerian-Eulerian multiphase model for non-equilibrium condensation in transonic steam flow," *International Journal of Heat and Mass Transfer,* pp. 2217-2231, 2004.

[12] W. Wróblewski, S. Dykas and A. Gepert, "Steam condensing flow modeling in turbine channels," *International Journal of Multiphase Flow,* vol. 35, pp. 498-506, 2009.

[13] S. Dykas and W. Wróblewski, "Single- and two-fluid models for steam condensing flow modeling," *International Journal of Multiphase Flow,* vol. 37, pp. 1245-1253, 2011.

[14] C. Brennen, Cavitation and Bubble Dynamics, Oxford University Press, 1995.

[15] F. Bakhtar, J. B. Young, A. J. White and D. A. Simpson, "Classical nucleation theory and its application to condensing steam flow calculations," in *Proceedings of the Institution of Mechanical Engineers, Part C: Journal of Mechanical Engineers Science*, 2005.

[16] A. Kantrovitz, "Nucleation in very rapid vapour expansions," *J. Chem. Phys.,* vol. 19, pp. 1097-1100, 1951.

[17] F. Mazzelli, Single & Two-Phase Supersonic Ejectors for Refrigeration Applications, Florence: Ph.D. Thesis, 2015.

[18] J. B. Young, "The Spontaneous Condensation in Supersonic Nozzles," *PhysicoChemical Hydrodynamics,* vol. 3, no. 1, pp. 57-82, 1982.

[19] International Assotiation for the Properties of Water and Steam, "Thermophysical Properties of Metastable Steam and Homogeneous Nucleation," 2011.

[20] J. B. Young, "An Equation of State for Steam for Turbomachinery and Other Flow Calculations," *Journal of Engineering for Gas Turbines and Power,* vol. 110, no. 1, pp. 1-7, 1988.

[21] E. Lemmon, M. Huber and M. McLinden, "NIST Standard Reference Database 23: Reference Fluid Thermodynamic and Transport Properties-REFPROP, Version 9.1," 2013.

[22] ANSYS Inc., ANSYS Fluent Theory Guide, Canonsburg, PA: release 18.0, 2016.

[23] M. Labois and C. Narayanan, "Non-conservative pressure-based compressible formulation for multiphase flows with heat and mass transfer," in *9th International Conference on Multiphase Flow*, May 22nd - 27th, Firenze, Italy, 2016.

[24] L. Zori and F. Kelecy, "Wet Steam Flow Modeling in a General CFD Flow Solver," in *35th AIAA Fluid Dynamics Conference and Exhibit*, Toronto, Ontario, Canada, 6 - 9 June 2005.

[25] Y. Yang and S. Shen, "Numerical simulation on non-equilibrium spontaneous condensation," *International Communications in Heat and Mass Transfer ,* vol. 36, pp. 902-907, 2009.

[26] B. Leonard, "A stable and accurate convective modelling procedure based on quadratic upstream interpolation," *Computer Methods in Applied Mechanics and Engineering,* vol. 19, pp. 59-98, 1979.

[27] G. Gyarmathy, "Bases for a theory for wet steam turbines," PhD thesis, ETH Zurich, 1962.

[28] M. Joswiak, N. Duff, M. Doherty and B. Peters, "Size-Dependent Surface Free Energy and Tolman-Corrected Droplet Nucleation of TIP4P/2005 Water," *J. Phys. Chem. Lett. ,* vol. 4, p. 4267−72, 2013.

[29] F. R. Menter, "Two-Equation Eddy-Viscosity Turbulence Models for Engineering Applications," *AIAA Journal,* vol. 32, no. 8, pp. 1598-1605, 1994.

[30] F. Mazzelli, A. B. Little, S. Garimella and Y. Bartosiewicz, "Computational and Experimental Analysis of Supersonic Air Ejector: Turbulence Modeling and Assessment of 3D Effects," *International Journal of Heat and Fluid Flow,* vol. 56, pp. 305-316, 2015.

[31] F. Mazzelli and A. Milazzo, "Performance analysis of a supersonic ejector cycle," *International Journal of Refrigeration,* vol. 49, pp. 79-92, 2015.

[32] F. Hughes, J. Starzmann, A. White and Y. J.B., "A Comparison of Modeling Techniques for Polydispersed Droplet Spectra in Steam Turbines," *Journal of Engineering for Gas Turbines and Power,* vol. 138, 2016.

[33] H. Ikawa, Turbulent Mixing Layer in Supersonic Flow, Ph.D. thesis, California Institute of Technology, 1973.

[34] G. Brown and A. Roshko, "On density effects and large structure in turbulent mixing layers," *journal of Fluid Mechanics ,* vol. 64, pp. 775-816, 1974.

[35] A. Smits and J.-P. Dussauge, Turbulent Shear Layers in Supersonic Flow, second edition, New York, NY: Springer, 2006.

[36] T. Gatsky and J.-P. Bonnet, Compressibility, Turbulence and High Speed Flow, 2nd edition, Oxford, UK.: Academic Press, 2013.

[37] D. Wilcox, "Dilatation–dissipation corrections for advanced turbulence models," *AIAA Journal,* vol. 11, pp. 2639-2646, 1992.

[38] D. Wilcox, Turbulence Modeling for CFD, La Canada, California: DCW Industries, Inc, 2006.

[39] C. Crowe, J. Schwarzkopf, M. Sommerfeld and Y. Tsuji, Multiphase flows with droplets and particles, second edition, Boca Raton, FL: CRC Press, 2012.

[40] H. R. Pruppacher, "A new look at homogeneous ice nucleation in supercooled water drops," *J. Atmos. Sci. ,* vol. 52, pp. 1924-33, 1995.

[41] J. Wölk, B. Wyslouzil and R. Strey, "Homogeneous nucleation of water: From vapor to supercooled droplets to ice," *AIP Conf. Proc.,* vol. 1527, pp. 55-62, 2013.

[42] The International Association for the Properties of Water and Steam, "Revised Release on Surface Tension of Ordinary Water Substance," IAPWS report, 2014.

1126
1127